

Evaporation-triggered microdroplet nucleation and the four life phases of an evaporating Ouzo drop

Huanshu Tan^a, Christian Diddens^b, Pengyu Lv^a, J. G. M. Kuerten^{b,c}, Xuehua Zhang^{d,1}, and Detlef Lohse^{a,e,1}

^aPhysics of Fluids Group, Department of Science and Technology, Mesa+ Institute, and J. M. Burgers Centre for Fluid Dynamics, University of Twente, 7500 AE Enschede, The Netherlands; ^bDepartment of Mechanical Engineering, Eindhoven University of Technology, 5600 MB Eindhoven, The Netherlands; ^cDepartment of Electrical Engineering, Mathematics, and Computer Science, University of Twente, 7500 AE Enschede, The Netherlands; ^dSoft Matter & Interfaces Group, School of Engineering, Royal Melbourne Institute of Technology University, Melbourne, VIC 3001, Australia; and ^eMax Planck Institute for Dynamics and Self-Organization, 37077 Goettingen, Germany

Edited by Michael P. Brenner, Harvard University, Cambridge, MA, and accepted by Editorial Board Member John D. Weeks June 1, 2016 (received for review February 10, 2016)

Evaporating liquid droplets are omnipresent in nature and technology, such as in inkjet printing, coating, deposition of materials, medical diagnostics, agriculture, the food industry, cosmetics, or spills of liquids. Whereas the evaporation of pure liquids, liquids with dispersed particles, or even liquid mixtures has intensively been studied over the past two decades, the evaporation of ternary mixtures of liquids with different volatilities and mutual solubilities has not yet been explored. Here we show that the evaporation of such ternary mixtures can trigger a phase transition and the nucleation of microdroplets of one of the components of the mixture. As a model system, we pick a sessile Ouzo droplet (as known from daily life—a transparent mixture of water, ethanol, and anise oil) and reveal and theoretically explain its four life phases: In phase I, the spherical cap-shaped droplet remains transparent while the more volatile ethanol is evaporating, preferentially at the rim of the drop because of the singularity there. This leads to a local ethanol concentration reduction and correspondingly to oil droplet nucleation there. This is the beginning of phase II, in which oil microdroplets quickly nucleate in the whole drop, leading to its milky color that typifies the so-called “Ouzo effect.” Once all ethanol has evaporated, the drop, which now has a characteristic nonspherical cap shape, has become clear again, with a water drop sitting on an oil ring (phase III), finalizing the phase inversion. Finally, in phase IV, all water has evaporated, leaving behind a tiny spherical cap-shaped oil drop.

ternary droplet evaporation | Ouzo effect | sessile droplets | different volatilities | nucleation

A coffee drop evaporating on a surface leaves behind a roundish stain (1). The reason lies in the pinning of the drop on the surface, together with the singularity of the evaporation rate at the edge of the drop, toward where the colloidal particles of the drop are thus transported. This so-called “coffee-stain effect” has become paradigmatic for a whole class of problems, and nearly 20 y after Deegan et al. (1) presented it to the scientific community, still various questions are open and the problem and its variations keep inspiring the community (1–18).

What happens when an Ouzo drop is evaporating? The Greek drink Ouzo (or the French Pastis or the Turkish Raki) consists of an optically transparent ternary mixture of water, ethanol, and anise oil. When served, water is often added, leading to the nucleation of many tiny oil droplets, which give the drink its milky appearance. This is the so-called Ouzo effect (19). As we will see in this paper, this problem can also become paradigmatic because of its extremely rich behavior, now for the evaporation-triggered phase separation of ternary liquids and droplet nucleation therein.

The reason for the Ouzo effect lies in the varying solubility of oil in ethanol–water mixtures: With increasing water concentration during the solvent exchange (i.e., water being added), the oil solubility decreases, leading to droplet nucleation in the bulk and—if present—also on hydrophobic surfaces (so-called surface nano-droplets) (20, 21).

Experiments and Numerical Modeling

Series of Events During Evaporation of a Sessile Ouzo Droplet and Their Interpretation. When an Ouzo drop is evaporating, the Ouzo effect is locally triggered by the preferred evaporation of the more volatile ethanol compared with the less volatile water and the even less volatile oil. As the evaporation rate is highest at the rim of the drop (6), we expect the oil microdroplets to nucleate there first. Indeed, this is what we see in our experiments, in which we have deposited a 1- μ L Ouzo drop on a transparent hydrophobic octadecyltrichlorosilane (OTS)-glass surface, monitoring its evaporation under ambient conditions with optical imaging synchronized from the top and side (Fig. 1, experimental set-up sketch in Fig. S1, and Movies S1 and S2), from the bottom (Fig. 2 and Movie S3), and confocally (Fig. 3 and Movies S4 and S5). For an illustration of the evaporation process see Fig. 4. At early times, the Ouzo drop is transparent and has a spherical cap shape (Fig. 1A). This is phase I of the evaporation process. After about 20 s, indeed microdroplets nucleate at the rim of the drop, as seen in Figs. 2B and 3B. This process signals the onset of phase II, sketched in Fig. 4A: The microdroplets are convected throughout the whole Ouzo drop, giving it its “milky” appearance (Fig. 1B). Because of the declining ethanol concentration, the liquid becomes oil oversaturated (*Materials and Methods* and Fig. S2). This oil oversaturation leads to further oil droplet growth (22) and coalescence (Fig. 2C). Finally, an oil ring appears, caused by the deposition of coalesced oil microdroplets on the surface (Figs. 1C, 2D, 3A, and sketch in Fig. 4B). The zoomed-in graphs in Figs. 2D and 3A reveal the presence of three contact lines (CL) near the oil ring: CL-1, where

Significance

The evaporation of an Ouzo droplet is a daily life phenomenon, but the outcome is amazingly rich and unexpected: Here we reveal the four different phases of its life with phase transitions in-between and the physics that govern this phenomenon. The Ouzo droplet may be seen as a model system for any ternary mixture of liquids with different volatilities and mutual solubilities. Our work may open up numerous applications in (medical) diagnostics and in technology, such as coating or for the controlled deposition of tiny amounts of liquids, printing of light-emitting diode (LED) or organic LED devices, or phase separation on a submicron scale.

Author contributions: H.T., X.Z., and D.L. designed research; H.T., C.D., P.L., and J.G.M.K. performed research; H.T., C.D., J.G.M.K., and D.L. analyzed data; and H.T., C.D., and D.L. wrote the paper.

The authors declare no conflict of interest.

This article is a PNAS Direct Submission. M.P.B. is a guest editor invited by the Editorial Board.

¹To whom correspondence may be addressed. Email: d.lohse@utwente.nl or xuehua.zhang@rmit.edu.au.

This article contains supporting information online at www.pnas.org/lookup/suppl/doi:10.1073/pnas.1602260113/-DCSupplemental.

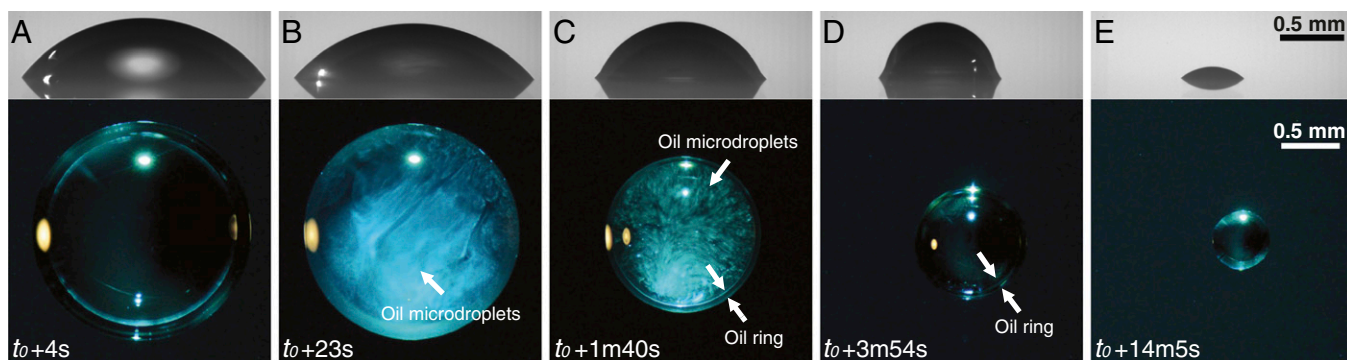


Fig. 1. Experimental snapshots during the evaporation of an “Ouzo” drop on a flat surface. The initial volume of the drop is $0.7 \mu\text{L}$ with an initial composition of 37.24% (wt/wt) water, 61.06% (wt/wt) ethanol, and 1.70% (wt/wt) anise oil (a mixture we refer to as Ouzo) in terms of weight fractions. The time t_0 is defined as the moment the needle was pulled out of the drop. A time series of the evaporation process can be seen in [Movies S1](#) and [S2](#). (A) At early times, the Ouzo drop is transparent and has a spherical-cap shape. (A, Bottom) The light ring and spots in the image are caused by reflection and refraction of the light source. (B) A color transition arises as a result of the Ouzo effect (i.e., the nucleation of nano- to micro-sized oil droplets, which are convected by the flow inside the Ouzo drop). The scattering of light at the nucleated microdroplets leads to the milky coloring of the drop. (C) The Ouzo drop loses its spherical cap shape due to the appearance of an oil ring. The complex transitions from A to C happen within 2.5 min, a short time compared with the whole process. (D) The Ouzo drop is transparent again. Oil microdroplets in the bulk grow big enough to sit on the surface or directly merge with the oil ring by convection. (E) After around 14 min of evaporation, only anise oil is left, now in a spherical cap shape again.

mixture, surface, and oil meet; CL-2, where mixture, oil, and air meet; and CL-3, where oil, substrate, and air meet. The drop is still opaque due to the presence of the numerous oil microdroplets in the bulk. However, after about 4 min all ethanol has evaporated. In this phase III, most of the oil droplets have coalesced to an oil ring at the rim of the drop, which now is transparent again (Figs. 1D, 2E, 3C, and sketch in Fig. 4C). In this now phase-inverted phase the drop has a very characteristic nonspherical cap shape, with a water drop sitting on an oil ring. Subsequently, the water drop evaporates more and more. The last traces of water are seen as water microdroplets in the bulk of the remaining spherical-cap-shaped sessile oil drop (Fig. 2F, phase IV), which now again has a single contact line. After around 14 min of evaporation, only a tiny sessile oil droplet is left (with 1/70th of the original drop volume), now in spherical cap shape again (Fig. 1E and sketch in Fig. 4D).

The four life phases of the evaporating Ouzo drop not only are seen visually, but also reflect various quantitative measures of

the drop geometry, extracted from the images in Figs. 1 and 2, according to the procedure described in [Supporting Information](#) and [Fig. S3](#). In Fig. 5 A–D we show the measured drop volume $V(t)$ its contact diameter $L(t)$, and the diameter $L^*(t)$ of the water drop sitting on the oil ring; the corresponding contact angles $\theta(t)$ and $\theta^*(t)$; and the radius of curvature $R(t)$ of the drop. The four characteristic phases are separated by three black vertical dashed lines: phase I, before the Ouzo effect starts (i.e., before the microdroplets are optically observed at the rim of the drop); phase II, before all ethanol in the drop has evaporated, which is determined from a force balance analysis at CL-2 as detailed in [Materials and Methods](#); phase III, before the water in the drop has evaporated [i.e., before $\theta(t)$ approaches the contact angle of pure anise oil]; and phase IV, when the drop consists of oil only.

After ~ 60 s, the oil ring appeared, which is indicated in Fig. 5 as a green vertical solid line. From that moment, the evolution of the two additional geometrical parameters L^* and θ^* is shown.

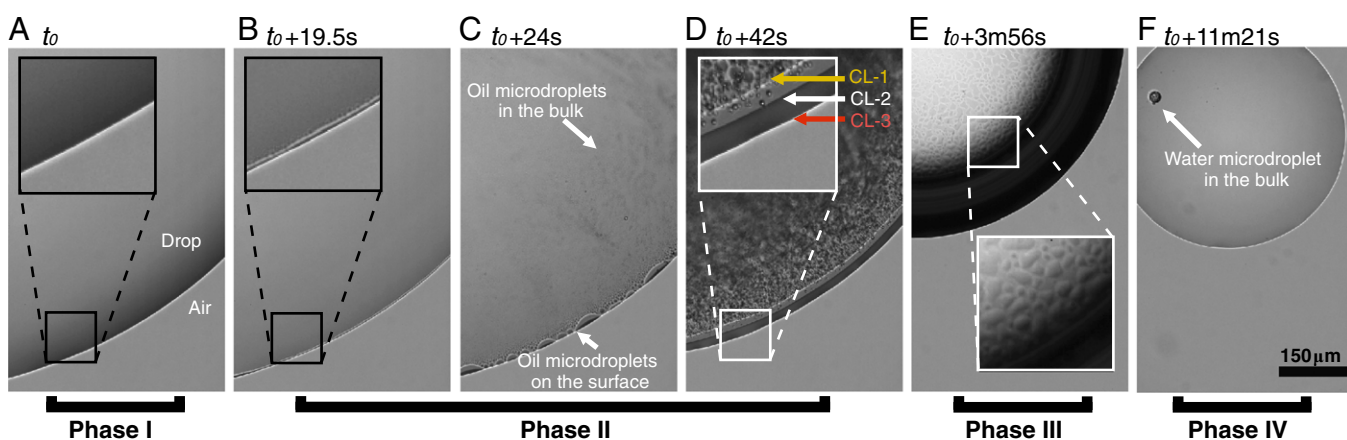


Fig. 2. Bottom-view snapshots of the contact region of an evaporating $0.7\text{-}\mu\text{L}$ Ouzo drop of the same composition as in Fig. 1 ([Movie S3](#)). (A) Phase I: The Ouzo drop is totally transparent with a clearly defined CL. (B) Phase II: After around 20 s, the CL is thickened due to the nucleation of oil microdroplets at the rim as shown in the zoomed-in graph. (C) Oil microdroplets nucleated near the CL are convected throughout the entire drop. Meanwhile, the oil microdroplets at the CL grow and coalesce. (D) An oil ring has appeared, caused by the deposition of coalesced oil microdroplets on the surface. D, Inset reveals the presence of three CLs, CL-1, CL-2, and CL-3 near the oil ring, as explained in the main text. The drop is opaque because of the presence of numerous oil microdroplets in the bulk. (E) Phase III: The outer diameter of the oil ring is smaller, whereas the thickness is much larger. The drop has become transparent again and many merged oil microdroplets on the surface can be observed. (F) The drop is transparent with a single CL, CL-3. A water microdroplet has been produced as a residual of CL-2. Finally, this remaining water dissolves into the oil and disappears, leaving a homogeneous oil drop (phase IV). (Insets: $\sim 2.5\times$ magnification.)

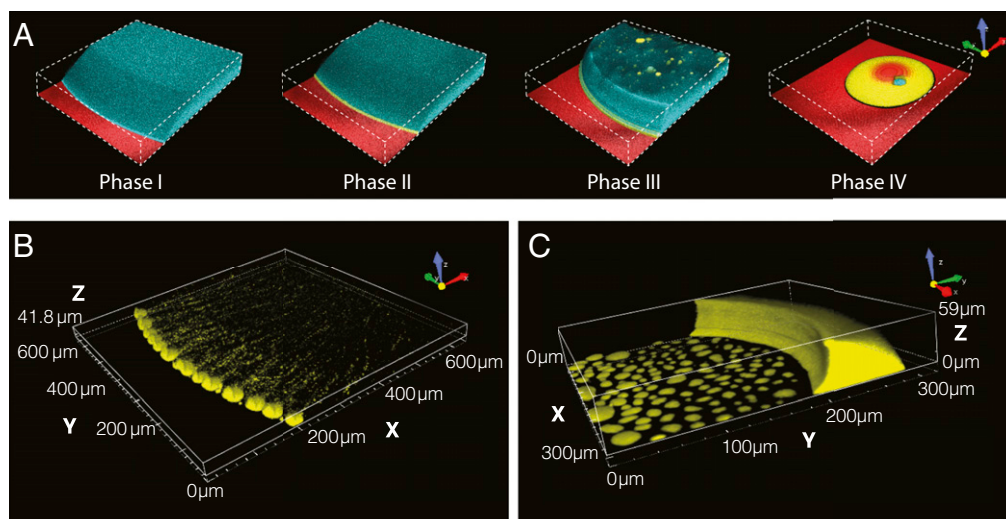


Fig. 3. Confocal images of the Ouzo drop in different phases. A water–ethanol solution (blue) and oil (yellow) were labeled with different dyes in the confocal experiment. (A) Morphology of the evaporating Ouzo drop corresponding to four different life phases, taken from a confocal view (Movie S4). The scan volume of the confocal microscope is $560\ \mu\text{m} \times 560\ \mu\text{m} \times 90\ \mu\text{m}$. (B) The coalesced oil microdroplets on the surface and fresh nucleated oil microdroplets in the bulk were presented in 3D at $t_0 + 26\ \text{s}$ (early in phase II). For the appropriate spatial resolution the 3D images had to be taken over a period of 0.9 s, leading to motion blur of the moving oil microdroplets. (C) As the oil ring shrinks over time, surface oil microdroplets are destined to be absorbed as shown at $t_0 + 374\ \text{s}$ (early in phase III). Confocal Movie S5 shows the early nucleation process.

In phases I and II, $V(t)$ and $L^*(t)$ decrease very fast, due to the high evaporation rate of ethanol. Once all ethanol has evaporated, at the transition from phase II to phase III, there is a sharp reduction in the slopes of $V(t)$, $L^*(t)$, and $R(t)$, which in phase-inverted phase III decrease more slowly due to the lower evaporation rate of water. In this regime, a force balance holding at CL-2 reaches its steady state (Fig. S4). In the final phase, $V(t)$ converges to the initial volume of the anise oil (Fig. 5A, Inset) and $\theta(t)$ approaches the contact angle of pure anise oil (Fig. 5C).

Numerical Modeling of the Evaporation Process and Its Quantitative Understanding. More quantitative insight is gained from numerically modeling the evaporation process of the Ouzo drop (Movie S6). Our numerical model is based on an axisymmetric lubrication approximation in the spirit of the evaporating coffee-stain lubrication models of refs. 1, 5, 15, and 23, but now for a multicomponent liquid. The relative mass fractions are governed by a convection–diffusion equation, with a sink term at the air–drop interface, reflecting evaporation and ethanol-concentration-dependent material parameters such as density, diffusivity, viscosity, surface tension, and activity coefficients (quantifying the evaporation rate). These composition-dependent properties are depicted in Fig. S5. The Ouzo drop is described assuming axial symmetry, with the liquid–air interface given by the height function $h(r,t)$ and the fluid velocity $\vec{v} = (u, w)$ (Fig. S6). Details of the model are given in Supporting Information.

The fundamental difference between the evaporation of a pure liquid (23) and that of a mixture is the vapor–liquid equilibrium. Whereas in the case of a pure liquid α the vapor concentration c_α (mass per volume) directly above the liquid–air interface is saturated (i.e., $c_\alpha = c_{\alpha,\text{sat}}$), it is lower for the case of mixtures. The relation between liquid composition and vapor composition is expressed by Raoult’s law. As in the evaporation model for a pure liquid (23), the evaporation rate J_α is obtained by solving the quasi-steady vapor diffusion $\nabla^2 c_\alpha = 0$ in the gas phase with the boundary conditions given by Raoult’s law above the drop, by the no-flux condition $\partial_z c_\alpha|_{r>L/2, z=0} = 0$ at the drop-free substrate, and far away from the drop by the given vapor concentrations $c_\alpha = 0$ for ethanol and $c_\alpha = c_{\alpha,\infty} = \text{RH}_\alpha c_{\alpha,\text{sat}}$ for water, where RH_α is the relative humidity. The relative humidity can be measured to some limited precision, but here had to be corrected for to better describe the

experimental data, as detailed in Materials and Methods. Finally, the evaporation rates are given by $J_\alpha = -D_{\alpha,\text{air}} \partial_n c_\alpha$ with the vapor diffusion coefficients $D_{\alpha,\text{air}}$ of α in air. In contrast to the evaporation of a pure fluid, the evaporation rate of a mixture component depends not only on the geometric shape of the drop, but also on the entire composition along the liquid–air interface. The resulting r -dependent height loss resulting from evaporation is given in Supporting Information.

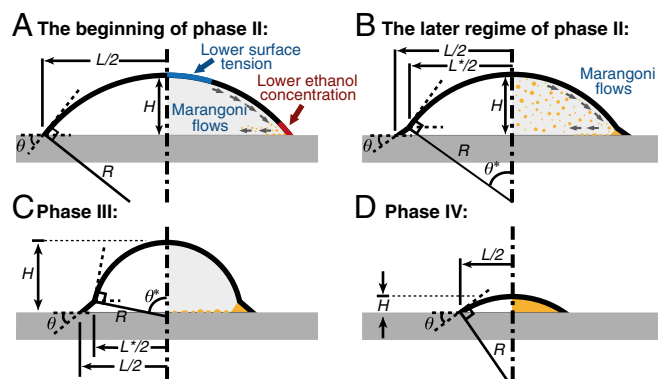


Fig. 4. Schematics of the Ouzo drop with the definitions of the geometrical parameters at four particular moments. (A) Because of the preferential evaporation of ethanol near the contact line, the nucleation of oil microdroplets starts in this region. The surface tension gradient drives a Marangoni flow that leads to a convection of the oil microdroplets. Despite the nonuniform surface tension, the contour of the drop is well described by a spherical cap with radius R . (B) At later times of regime phase II, the oil microdroplets are present in the entire drop and also cover the surface. Meanwhile, the oil ring (indicated by the orange triangular region) has appeared, which allows for the definition of two new geometrical parameters L^* and θ^* (C) After the ethanol content has completely evaporated, the main part of the drop consists of water only. The oil microdroplets in the bulk have coalesced and form a thicker oil ring and larger oil microdroplets on the substrate. Due to the relatively slow evaporation rate of water compared with ethanol, this stage lasts much longer than phase II. (D) Finally, only the nonvolatile oil remains after both ethanol and water have evaporated. The sessile drop now again has a spherical-cap shape.

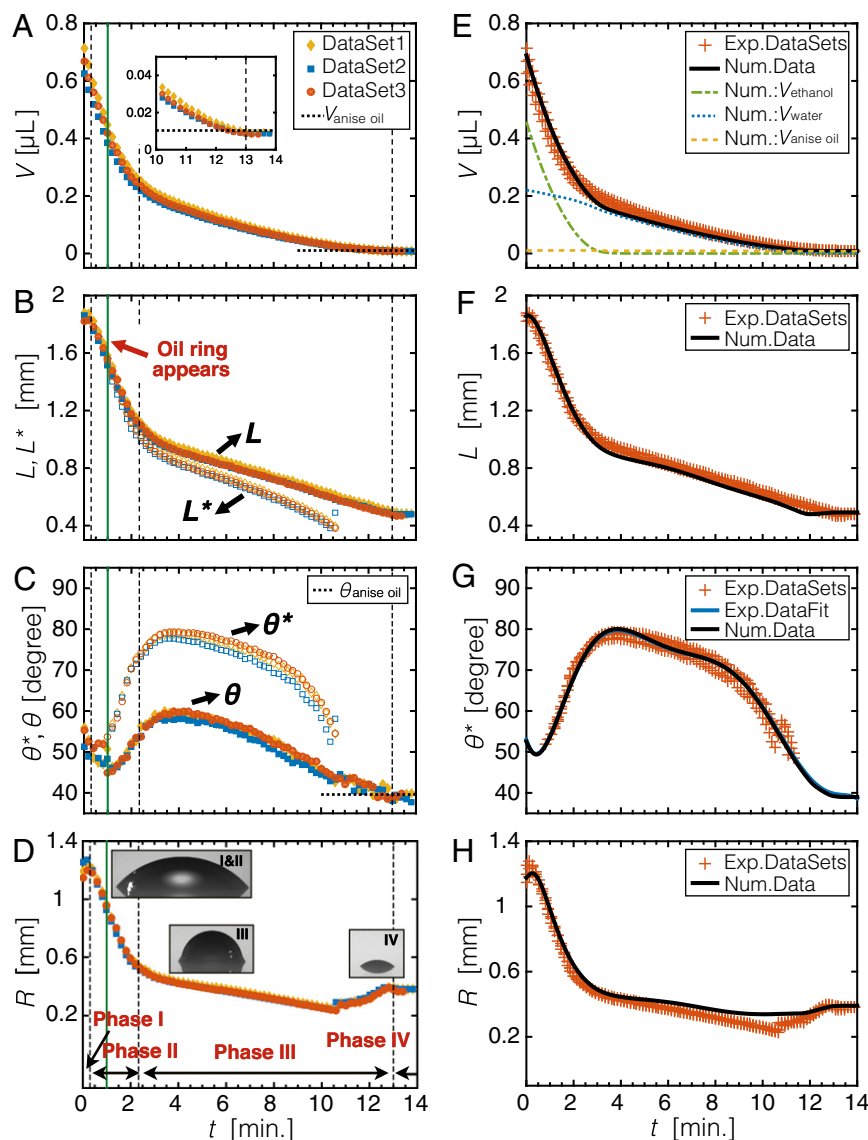


Fig. 5. Experimental (A–D) and numerical (E–H) results for the temporal evolution of the geometrical parameters: volume V (A and E), lateral sizes L and L^* (B and F), contact angles θ and θ^* (C and G), and radius of curvature R (D and H). The vertical dashed lines mark the transition from one phase to another.

In the simulations, the fitted experimental data θ^* (shown in Fig. 5G) were used as the time-dependent contact angle. The quantitative measures of the drop geometry resulting from the numerical simulations are shown in Fig. 5E, F, and H, together with the experimental data, showing excellent quantitative agreement. From Fig. 5E, which next to the total volume $V(t)$ also shows the partial volumes of the three components water, ethanol, and oil, we can reconfirm that the volume loss is initially mainly due to the evaporation of ethanol (phases I and II), followed by a slower evaporation of the remaining water (phase III). Finally, only the tiny nonvolatile oil droplet remains (phase IV).

Our numerical simulations of the process allow us to deduce the fully spatially resolved mass fraction and velocity fields, $y_a(r, z, t)$ and $\vec{v}(r, z, t)$, respectively. In Fig. 6A and B we show the ethanol mass fraction $y_e(r, z, t)$ and the velocity field $\vec{v}(r, z, t)$ for two different times $t = 20$ s and $t = 180$ s. It is clearly visible how the preferential evaporation of ethanol near the contact line, which leads to a larger surface tension there, drives a fast Marangoni flow. As a consequence, ethanol is quickly replenished at the liquid–air interface and can completely evaporate. We note that the direction of the

convection roll inside the drop is opposite to the case of a pure liquid, where the flow goes outward at the bottom of the drop and inward at the liquid–gas interface (1, 15, 23). We also note that the ethanol concentration differences are relatively small—in the beginning about 3% (wt/wt) and later not more than 0.5%—but nonetheless sufficient to drive a strong Marangoni flow with velocities up to the order of 10 mm/s. Due to the high contact angle during phases II and III, the lubrication approximation predicts the precise values of the velocity only to a limited accuracy. The qualitative flow field and the order of magnitude, however, have been validated by a comparison with the corresponding nonapproximated Stokes flow at individual time steps. Fig. 6C shows the water mass fraction $y_w(r, z, t)$ for $t = 46.5$ s, because at these later times ethanol is virtually not present anymore, again together with the velocity field, which is now again outward directly above the substrate.

Finally, in Fig. 6D we show the oil droplet nucleation time t_{nuc} , which is defined as the moment when the local composition crosses the phase separation curve and enters the Ouzo region (Fig. S24). According to the numerical results, the oil droplet nucleation starts at 20 s near the contact line, in perfect

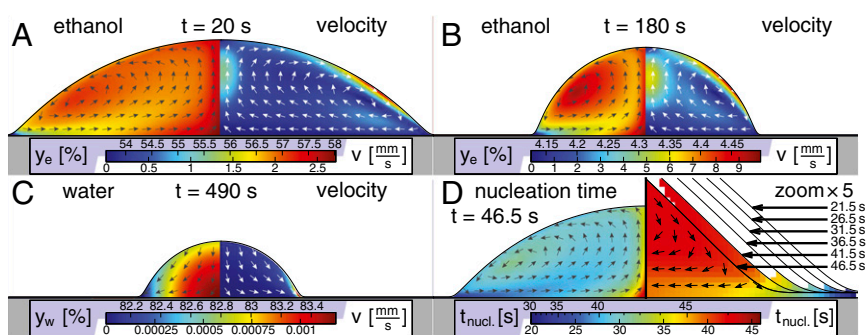


Fig. 6. (A–C) Snapshots of the numerical results at three different times $t = 20$ s (A), $t = 180$ s (B), and $t = 490$ s (C). (A and B) Mass fraction of ethanol $y_e(r, z, t)$ and fluid velocity field $\vec{v}(r, z, t)$, whose direction is indicated by the arrows and whose modulus by the color code. At the later time $t = 490$ s in C, the water concentration is plotted instead of the ethanol concentration (which then is close to zero), again together with the velocity field. (D) Oil droplet nucleation time t_{nucl} . *Right* shows a zoom-in of the region around the rim. **Movie S6** shows the numerical simulation.

agreement with our experimental findings, and nucleation is possible in the entire droplet at $t = 46.5$ s.

Conclusions and Outlook

In summary, we have experimentally and numerically studied the evaporation of a millimeter-sized sessile Ouzo drop on a hydrophobic substrate. How stimulating it can be to study the evaporation of alcoholic drinks has interestingly also been shown in a very recent parallel but independent work by Kim et al. (24), who studied the drying of whiskey droplets, which give a uniform deposition pattern. For that system suspended material and surface-absorbed macromolecules play a major role and offer a physicochemical avenue for the control of coatings. From our point of view, just as the evaporating whiskey droplet, also the evaporating Ouzo droplet can advance our scientific understanding of complex flow phenomena and phase transitions and their interaction. In this paper we have observed evaporation-triggered phase transitions and the nucleation of oil microdroplets, first at the edge of the Ouzo drop and then all over, followed by a phase inversion, and altogether four different life phases of the Ouzo drop, which serves as a paradigmatic model system for ternary mixtures of liquids with different volatilities and mutual solubilities. Here, water as the second but most volatile liquid (after the very quickly evaporating ethanol) also evaporates in about 10 min, leaving behind a tiny drop of anise oil. For other ternary mixtures only one liquid may be volatile, implying phase III with a binary mixture, and nucleated microdroplets of one liquid and its peculiar optical properties would be the final state.

Tuning and optimizing the material and chemical properties of the individual liquids in the ternary mixture such as volatilities and mutual solubilities and polymerizability (e.g., under UV exposure such as in ref. 25) offer a plethora of applications for medical diagnostics, for the controlled deposition of complex liquids in the food and cosmetic industry, for coating applications (26–30), in agriculture or the food or cosmetics industry, for inkjet printing of light-emitting diode (LED) or organic LED devices and solar cells (31–35), and for rapid manufacturing. Here we studied the deposition on smooth surfaces, but pre patterning the surface with hydrophobic patches (36) offers even further opportunities, by directing the nucleation of nano- or microdroplets at will, allowing for the self-organized bottom-up construction of structures.

Materials and Methods

Ternary Diagram and Initial Composition of the Ouzo Drop. The ternary liquid of the Ouzo drop in this study was the mixture of Milli-Q water [produced by a Reference A+ system (Merck Millipore) at 18.2 M Ω ·cm (at 25°C)], ethanol (EMD Millipore; ethanol absolute for analysis), and anise oil (Aldrich; anise oil). The ternary diagram of the mixture was titrated at a temperature of 22 °C, which is similar to the environmental temperature during the evaporation experiment. Twenty-one groups of ethanol and anise oil mixtures with different component weight ratios were properly prepared to be used as titrants (Table S1).

The volume of water (titrate) was precisely measured by a motorized syringe pump (Harvard; PHD 2000). For each ethanol and anise oil mixture, a phase-separation point was determined as shown in Fig. S2A. Photographs of the macrosuspensions corresponding to the different phase-separation points were taken. Thereby, the stability of the macrosuspension along the phase separation curve was determined (Fig. S2B). Starting with point “g” in Fig. S2B, the homogeneous macrosuspension is not stable anymore. The part of the curve with a stable macrosuspension was identified as the boundary of the Ouzo region in the ternary diagram, which is labeled Ouzo range. According to the ternary diagram, the initial composition of the Ouzo drop was chosen as 37.24% (wt/wt) water, 61.06% (wt/wt) ethanol, and 1.70% (wt/wt) anise oil in terms of weight fractions, which is indicated by the black star in Fig. S2A. Starting from this initial point, the drop composition is guaranteed to cross the phase-separation curve and enter the Ouzo region during the evaporation process. A black dotted line in Fig. S2A, *Inset* shows the numerically obtained temporal evolution of the composition near the contact line of the Ouzo drop.

Experimental Methods. A 0.7- μ L Ouzo drop [37.24% (wt/wt) water, 61.06% (wt/wt) ethanol, and 1.70% (wt/wt) anise oil in terms of weight fractions] was produced through a custom needle [Hamilton; outer diameter/inner diameter (in millimeters): 0.21/0.11] by a motorized syringe pump (Harvard; PHD 2000). The whole evolution of the Ouzo drop was observed by two synchronized cameras, one [Photron Fastcam SA-X2 64 GB, 50 frames per second (fps) at 1,024 \times 1,024 pixel resolution] affixed with a high-magnification zoom lens system (Thorlabs; MVL12X3Z) for side-view recordings and another (Nikon D800E, 25 fps at 1,920 \times 1,080 pixel resolution) affixed with an identical lens system for top-view recordings (Fig. 1 and **Movies S1** and **S2**). The temperature around the evaporating drop was measured using a thermometer sensor. The relative humidity in the laboratory was measured with a standard hygrometer ($\pm 3\%$ RH for 35% \sim 70% RH at 20 °C). The temperature of the three experimental datasets in Fig. 5 was between 21 °C and 22.5 °C. The relative humidity was around 40%. The image analysis was performed by custom-made MATLAB codes. To have a detailed observation of the evolutionary process at the rim of the Ouzo drop, an inverted microscope (Olympus GX51) was used to focus on the contact region. A fast-speed camera (Photron Fastcam SA-X2 64 GB, 50 fps at 1,024 \times 1,024 pixel resolution) was connected to the microscope with an intermediate tube. Fig. 2 and **Movie S3** were taken with a 20 \times long working m-plan fluorite objective [Olympus MPLFLN20XB, working distance (WD) = 3.0 mm, NA = 0.45]. Besides 2D imaging, we also took advantage of a confocal microscope (Nikon Confocal Microscopes A1 system) in stereo-imaging. A real-time observation was carried out to monitor the movement of the oil droplets due to the convective flow and the formation of oil ring in a 3D view. A 20 \times air objective (CFI Plan Apochromat VC 20 \times 0.75 DIC, NA = 0.75, WD = 1.0 mm) and a 40 \times air objective (CFI Plan Fluor 40 \times 0.75 DIC, NA = 0.75, WD = 0.66 mm) were used for Fig. 3 A and B and Fig. 3C, respectively. In Fig. 3 B and C and **Movie S5**, anise oil was labeled by Nile Red (Microscopy grade; Sigma-Aldrich). In Fig. 3A and **Movie S4**, to simultaneously label oil and solution with different color dyes during the whole evaporating process, anise oil was replaced by trans-Anethole oil (99%; Sigma-Aldrich) labeled by perylene (sublimed grade, $\geq 99.5\%$; Sigma-Aldrich) in yellow color. The water–ethanol mixture was labeled by fluorescein 5(6)-isothiocyanate (high-performance liquid chromatography; Sigma-Aldrich) in blue color.

Definitions of the Four Life Phases of an Evaporating Ouzo Drop. We divided the Ouzo drop evaporation process into four phases: Phase I is defined as the initial regime, before the critical phase-separation composition is attained at the contact line. Phase II is the time from the initial occurrence of the oil nucleation until the complete evaporation of the ethanol component. Phase III is the regime when the remaining water amount in the drop evaporates. The final phase IV is the period after the remaining water has evaporated. The first gray vertical dashed line (separation between phases I and II) and the third one (separation of phases III and IV) in Fig. 5 were able to be optically determined from the top- or bottom-view movie recordings. However, the transition between phase II and phase III cannot be detected from the movie recordings. Instead, the second gray vertical dashed line in Fig. 5 was determined from an equilibrium analysis as a simplified model (compare with Fig. S4A): At the air-mixture-oil contact line (CL-2 in Figs. 2B and 3 A and C), a force balance holds. The influence of the line tension on the balance can be neglected (37). Each variation of the composition in the drop alters the equilibrium of this balance (37, 38). At the moment when ethanol has completely evaporated, this equilibrium attains its steady state. From that moment, the three phases that meet at CL-2 are water from the liquid of the drop, anise oil from the oil ring, and air from the surroundings. The composition of the air phase near CL-2 is assumed to be constant. Hence, the angle between the mixture-air interface and the oil-air interface has to be constant. Mathematically speaking, this means that $\Delta\theta$ has to be a constant. The quantity $\Delta\theta$ was estimated by the subtraction $\theta^* - \theta$ because the dimension of the oil-air interface is small in the initial part of phase III. In Fig. S4B, the evolution of $\Delta\theta$ as a function of time is shown. It is clearly visible that after a rapid increase $\Delta\theta$ remains constant for a very long time. Therefore, we fitted $\Delta\theta$ from time t_a to time $t_z = 480$ s by a constant c . Fig. S4B, Inset shows the relation between $c(t_a)$ and t_a . We selected the time $t_a = 140$ s as the separation moment between phase II and phase III.

Numerical Model. The evolution of the drop shape $h(r,t)$ (Fig. S6) is solved by a diagonally implicit Runge-Kutta method, the vapor diffusion-limited evaporation rates are calculated by a boundary element method, and the convection-diffusion equations for the composition are treated with an upwind finite differences scheme. For the composition dependency of the mass density, the surface tension, the diffusion coefficient, the viscosity, and the activity coefficients, we fitted experimental data of water-ethanol mixtures or used appropriate models (Fig. S5). Details can be found in Supporting Information. Our model was validated for the case of pure water by comparison with the experimental data of Gelderblom et al. (15).

Determination of the Relative Humidity. For the numerical simulation, we have assumed a temperature of $T = 21$ °C and a relative humidity of $RH_e = 0$ for ethanol. Because the experimental determination of the relative humidity RH_w of water is error prone, we have determined it as follows: At the beginning of phase III, the drop consists almost entirely of water, because the ethanol content has already evaporated and the amount of oil is still small in comparison with the remaining water volume. Therefore, we used our numerical model to fit RH_w based on the experimental data for the volume evolution $V(t)$ during the time from $t = 140$ s to $t = 300$ s. The resulting water humidity reads $RH_w = 63\%$.

ACKNOWLEDGMENTS. We thank Michel Versluis for invaluable advice on imaging and Shuhua Peng for preparing the substrates. This study was supported in part by a European Research Council Advanced grant (to D.L.); the NWO-Spinoza programme (D.L.); China Scholarship Council Grant 201406890017 (to H.T.); and the Dutch Technology Foundation STW (J.G.M.K. and C.D.). X.Z. acknowledges support from an ARC Future Fellowship (FFT120100473) and Discovery Program (DP140100805).

- Deegan RD, et al. (1997) Capillary flow as the cause of ring stains from dried liquid drops. *Nature* 389(6653):827–829.
- Picknett RG, Bexon R (1977) The evaporation of sessile or pendant drops in still air. *J Colloid Interface Sci* 61(2):336–350.
- Hu H, Larson RG (2002) Evaporation of a sessile droplet on a substrate. *J Phys Chem B* 106(6):1334–1344.
- Sefiane K, Tadrif L, Douglas M (2003) Experimental study of evaporating water-ethanol mixture sessile drop: Influence of concentration. *Int J Heat Mass Trans* 46(23):4527–4534.
- Popov YO (2005) Evaporative deposition patterns: Spatial dimensions of the deposit. *Phys Rev E Stat Nonlin Soft Matter Phys* 71(3 Pt 2B):036313.
- Cazabat A-M, Guena G (2010) Evaporation of macroscopic sessile droplets. *Soft Matter* 6(12):2591–2612.
- Shahidzadeh-Bonn N, Rafai S, Azouni A, Bonn D (2006) Evaporating droplets. *J Fluid Mech* 549:307–313.
- Ristenpart WD, Kim PG, Domingues C, Wan J, Stone HA (2007) Influence of substrate conductivity on circulation reversal in evaporating drops. *Phys Rev Lett* 99(23):234502.
- Lim JA, et al. (2008) Self-organization of ink-jet-printed triisopropylsilylethynyl pentacene via evaporation-induced flows in a drying droplet. *Adv Funct Mater* 18(2):229–234.
- Ming T, et al. (2008) Ordered gold nanostructure assemblies formed by droplet evaporation. *Angew Chem Int Ed* 47(50):9685–9690.
- Sefiane K, David S, Shanahan MER (2008) Wetting and evaporation of binary mixture drops. *J Phys Chem B* 112(36):11317–11323.
- Liu C, Bonaccorso E, Butt H-J (2008) Evaporation of sessile water/ethanol drops in a controlled environment. *Phys Chem Chem Phys* 10(47):7150–7157.
- Schönfeld F, Graf KH, Hardt S, Butt H-J (2008) Evaporation dynamics of sessile liquid drops in still air with constant contact radius. *Int J Heat Mass Transfer* 51(13-14):3696–3699.
- Christy JRE, Hamamoto Y, Sefiane K (2011) Flow transition within an evaporating binary mixture sessile drop. *Phys Rev Lett* 106(20):205701.
- Gelderblom H, et al. (2011) How water droplets evaporate on a superhydrophobic substrate. *Phys Rev E Stat Nonlin Soft Matter Phys* 83(2 Pt 2):026306.
- Marín AG, Gelderblom H, Lohse D, Snoeijer JH (2011) Order-to-disorder transition in ring-shaped colloidal stains. *Phys Rev Lett* 107(8):085502.
- Brutin D, Sobac B, Loquet B, Sampaol J (2011) Pattern formation in drying drops of blood. *J Fluid Mech* 667:85–95.
- Ledesma-Aguilar R, Vella D, Yeomans JM (2014) Lattice-Boltzmann simulations of droplet evaporation. *Soft Matter* 10(41):8267–8275.
- Vitale SA, Katz JL (2003) Liquid droplet dispersions formed by homogeneous liquid-liquid nucleation: "The ouzo effect". *Langmuir* 19(10):4105–4110.
- Zhang XH, Ducker W (2007) Formation of interfacial nanodroplets through changes in solvent quality. *Langmuir* 23(25):12478–12480.
- Lohse D, Zhang X (2015) Surface nanobubble and surface nanodroplets. *Rev Mod Phys* 87(3):981–1035.
- Zhang X, et al. (2015) Mixed mode of dissolving immersed nanodroplets at a solid-liquid interface. *Soft Matter* 11(10):1889–1900.
- Deegan RD, et al. (2000) Contact line deposits in an evaporating drop. *Phys Rev E Stat Phys Plasmas Fluids Relat Interdiscip Topics* 62(1 Pt B):756–765.
- Kim H, et al. (2016) Controlled uniform coating from the interplay of marangoni flows and surface-adsorbed macromolecules. *Phys Rev Lett* 116(12):124501.
- Zhang XH, et al. (2012) From transient nanodroplets to permanent nanolenses. *Soft Matter* 8(16):4314–4317.
- Hughes TR, et al. (2001) Expression profiling using microarrays fabricated by an ink-jet oligonucleotide synthesizer. *Nat Biotechnol* 19(4):342–347.
- Creran B, et al. (2014) Detection of bacteria using inkjet-printed enzymatic test strips. *ACS Appl Mater Interfaces* 6(22):19525–19530.
- Murphy SV, Atala A (2014) 3D bioprinting of tissues and organs. *Nat Biotechnol* 32(8):773–785.
- da Luz LL, et al. (2015) Inkjet printing of lanthanide-organic frameworks for anti-counterfeiting applications. *ACS Appl Mater Interfaces* 7(49):27115–27123.
- Yamada K, Henares TG, Suzuki K, Citterio D (2015) Paper-based inkjet-printed microfluidic analytical devices. *Angew Chem Int Ed* 54(18):5294–5310.
- Sirringhaus H, et al. (2000) High-resolution inkjet printing of all-polymer transistor circuits. *Science* 290(5499):2123–2126.
- de Gans BJ, Duineveld PC, Schubert US (2004) Ink jet printing of polymers: State of the art and future developments. *Adv Mater* 16(3):203–213.
- Williams C (2006) Ink-jet printers go beyond paper. *Phys World* 19(1):24–29.
- Dijksman JF, et al. (2007) Precision ink jet printing of polymer light emitting displays. *J Mater Chem* 17(6):511–522.
- Paul KE, Wong WS, Ready SE, Street RA (2003) Additive jet printing of polymer thin-film transistors. *Appl Phys Lett* 83(10):2070–2072.
- Bao L, Rezk AR, Yeo LY, Zhang X (2015) Highly ordered arrays of femtoliter surface droplets. *Small* 11(37):4850–4855.
- Torza S, Mason SG (1970) Three-phase interactions in shear and electrical fields. *J Colloid Interface Sci* 33(1):67–83.
- Bazhlekov IB, Shopov PJ (1997) Numerical simulation of dynamic contact-line problems. *J Fluid Mech* 352:113–133.
- Schwartz LW, Eley RR (1998) Simulation of droplet motion on low-energy and heterogeneous surfaces. *J Colloid Interface Sci* 202(1):173–188.
- Lee CY, Wilke CR (1954) Measurements of vapor diffusion coefficient. *Ind Eng Chem* 46(11):2381–2387.
- González B, Calvar N, Gómez E, Domínguez Á (2007) Density, dynamic viscosity, and derived properties of binary mixtures of methanol or ethanol with water, ethyl acetate, and methyl acetate at $t = (293.15, 298.15, \text{ and } 303.15)$ K. *J Chem Thermodyn* 39(12):1578–1588.
- Vazquez G, Alvarez E, Navaza JM (1995) Surface tension of alcohol water + water from 20 to 50 .degree.C. *J Chem Eng Data* 40(3):611–614.
- Páez S, Guevara-Carrion G, Hasse H, Vrabec J (2013) Mutual diffusion in the ternary mixture of water + methanol + ethanol and its binary subsystems. *Phys Chem Chem Phys* 15(11):3985–4001.
- Zuend A, Marcolli C, Luo BP, Peter T (2008) A thermodynamic model of mixed organic-inorganic aerosols to predict activity coefficients. *Atmos Chem Phys* 8(16):4559–4593.
- Zuend A, et al. (2011) New and extended parameterization of the thermodynamic model AIOMFAC: Calculation of activity coefficients for organic-inorganic mixtures containing carboxyl, hydroxyl, carbonyl, ether, ester, alkenyl, alkyl, and aromatic functional groups. *Atmos Chem Phys* 11(17):9155–9206.
- Lide DR, ed (2005) *CRC Handbook of Chemistry and Physics* (CRC Press, Boca Raton, FL).